Materials Advances

ROYAL SOCIETY OF CHEMISTRY

PAPER

View Article Online
View Journal

Check for updates

Cite this: DOI: 10.1039/d6ma00152a

Eosin Y-derived fluorescent sensors: selective Hg^{2+} detection and targeted biomedical applications

Biplove Kumar,[a] Venkatesh Muthukumar,[b] Arnab Chakraborty,[a] Asha Mahato,[a] Balaram Ghosh *[b] and Neeladri Das *[a]

Received 2nd February 2026,
Accepted 15th March 2026

DOI: 10.1039/d6ma00152a

rsc.li/materials-advances

Two eosin Y-based chemosensors (**EY-S$_O$**: λ_{em} = 534 nm and **EY-S$_M$**: λ_{em} = 551 nm) are synthesized for the selective, sensitive, and recyclable fluorescence "turn-on" detection of aquated Hg^{2+} ions. The quantum yield and fluorescence lifetime of the sensors were measured before and after analyte detection. Appreciable limits of detection (LOD: 6.01 ± 0.57 and 5.93 ± 0.09 nM, respectively) are observed. Optimal sensing occurs in neutral to slightly basic pH aqueous solutions. A selective Hg^{2+} detection mechanism is proposed based on experimental evidence. For the first time, the anticancer activities of eosin Y-based chemosensors (**EY-S$_O$** and **EY-S$_M$**) and their Hg^{2+} complexes (**EY-M$_O$** and **EY-M$_M$**) are studied. The anticancer activities of the complexes are significantly higher than those of their respective organic precursors or mercuric ions. The complexes are more effective against certain cancer cell lines relative to healthy cells. The IC_{50} of **EY-M$_M$** is 3.85 ± 0.306 μM against MDA-MB-231 and >50 μM against HEK-293 under similar experimental conditions. Various assays, including ROS generation, live/dead fluorescence imaging, and Annexin V-FITC/PI dual-staining, confirmed the underlying cell death pathways. Overall, we describe a facile approach to convert toxic Hg^{2+} species into two potent anticancer agents (**EY-M$_O$** and **EY-M$_M$**) for biomedical applications using two biocompatible chemosensors (**EY-S$_O$** and **EY-S$_M$**).

Introduction

Mercury detection plays a pivotal role in contemporary analytical science, driven by the element's formidable toxicity and its insidious tendency to biomagnify across trophic levels of different food chains in ecosystems. Even at ultra-trace concentrations, mercury has deleterious effects on the neurological, renal, and developmental systems of humans.[1,2] Consequently, there is continued research interest in developing techniques for the precise and timely monitoring of mercuric ions in the environment. In this context, fluorescent chemosensors have emerged as elegant and powerful tools, offering unparalleled sensitivity, molecular selectivity, and real-time responsiveness. Their practical use helps safeguard ecological integrity and public health from the toxic effects of mercuric ions.

In the present context, mercury sensing can be achieved using advanced materials such as metal–organic frameworks (MOFs), organic fluorophores, and carbon dots. MOFs offer tunable porosity and structural versatility; carbon dots are biocompatible and cost-effective, while organic fluorophores provide precise, responsive fluorescence signaling.[3–8] Among the described materials, the development of discrete fluorescent organic sensors is most popular among contemporary chemists because of their facile, high-yield synthesis, strong emissions, and superior selectivity toward Hg^{2+} ions. The modular design and adaptability of organic fluorescent sensors render these materials exceptionally well-suited for rapid and sensitive mercury detection in various environmental and biomedical settings, supporting advanced applications in pollution control, diagnostics, and emerging theranostic technologies.[9]

Owing to their structural diversity, tunable photophysical properties, and operational versatility, organic fluorescent sensors have emerged as the most efficient strategic materials for the selective detection of ultra-trace quantities of mercury ions (Hg^{2+}) in aqueous environments. A wide array of molecular scaffolds, including but not limited to xanthenes,[10–12] coumarins,[13–18] naphthalimides,[19,20] BODIPY dyes,[21–25] Schiff

---

[a] *Department of Chemistry, Indian Institute of Technology Patna, Patna 801106, Bihar, India. E-mail: neeladri@iitp.ac.in, neeladri2002@yahoo.co.in*

[b] *Epigenetic Research Laboratory, Department of Pharmacy, Birla Institute of Technology and Science-Pilani, Hyderabad Campus, Jawahar Nagar, Kapra Mandal, Medchal District, Telangana 500078, India. E-mail: balaram@hyderabad.bits-pilani.ac.in*

bases,[26–28] and thiourea derivatives,[29–32] have been incorporated to construct these molecular sensors, each offering distinct advantages in terms of sensitivity, selectivity, and emission characteristics. The fluorescence sensing mechanisms typically involve photoinduced electron transfer (PET),[33] internal charge transfer (ICT),[34] or specific metal–ligand coordination, enabling efficient and rapid recognition of Hg^{2+} ions.[35]

Naphthalimide, coumarin, and BODIPY-based molecules provide enhanced photostability and tunable emission profiles.[36–38] Schiff base and thiourea-functionalized sensors exhibit high affinity for mercuric (Hg^{2+}) ions through favourable soft–soft interactions, contributing to their high selectivity and sensitivity.[39,40] Xanthene-based sensors are particularly known for rapid and visually discernible fluorescence responses. For example, rhodamine derivatives are often associated with sharp ''off–on'' fluorescence responses and prominent colorimetric shifts upon mercury binding.[41] Hence, xanthene-based sensors are developed for real-time monitoring of the presence of mercuric ions in both environmental and biological contexts.[42–44]

Between ''turn-on'' and ''turn-off'' fluorescence sensing strategies, the former offers significant analytical advantages by suppressing background interference and activating signal output only upon specific analyte interaction. This reduces false negatives and enhances the signal clarity of the molecular sensor. Recent advances in the development of ratiometric probes, biocompatible sensor platforms, and dual-mode detection systems have further expanded the applicability of organic fluorescent sensors, and these are now integrated into various environmental surveillance and biomedical diagnostic frameworks.[45–48]

Turn-on fluorescence in metal ion sensing is often associated with the generation of reactive oxygen species (ROS), which enhances detection sensitivity and enables real-time imaging in biological systems. For example, Hg^{2+} can induce oxidative stress, leading to the formation of ROS that activate specific fluorophores, such as thiol- or boronate-based sensors.[49–52] Similarly, Fe^{2+} generates hydroxyl ($^{\bullet}OH$) radicals *via* Fenton chemistry, triggering fluorescence in ROS-sensitive probes.[53] Photoactive metal complexes, such as Ru(II), produce singlet oxygen ($^1O_2$) upon irradiation, enabling simultaneous metal sensing and ROS-based imaging or therapy in environmental and biomedical applications.[54] Fluorescent ROS-responsive molecules are considered to redefine theranostics by merging cancer imaging and therapy with antimicrobial action. Upon light activation, these molecules generate ROS, inducing mitochondrial damage and apoptosis in cancer cells, while their intrinsic fluorescence enables real-time tumor visualization.[55–58] Simultaneously, the oxidative stress produced assists in disrupting microbial membranes, offering potent antibacterial effects.[59,60] Fluorophores like porphyrins, BODIPY dyes, ruthenium(II) complexes, and rhodamine derivatives have been reported to demonstrate this dual role of serving as both diagnostic markers and therapeutic agents. By exploiting redox imbalances in diseased environments, these multifunctional molecules enable targeted, image-guided interventions, pushing the boundaries of precision medicine in oncology and infectious disease management.[61–65]

Inspired by previous research on fluorescent molecules, herein we report the development of two novel fluorescent sensors (**EY-S$_O$** and **EY-S$_M$**) through the facile coupling of commercially available and relatively inexpensive Eosin Y with halogen-substituted benzaldehyde derivatives. These molecular sensors exhibited outstanding selectivity, sensitivity, and recyclability in detecting mercury(II) ions present in aqueous solutions. Expanding their application, anticancer activities were assessed against the proliferation of MDA-MB-231 and A549 cancer cell lines, as well as normal HEK-293 cells. The mercury(II) complexes of the sensors (**EY-S$_O$** and **EY-S$_M$**) displayed potent cytotoxicity toward cancer cells with high selectivity indices, indicating low toxicity to normal cells. This dual functionality underscores the potential of these sensors not only for environmental monitoring but also as promising candidates for cancer therapeutic agents.

Materials and methods

Eosin Y, hydrazine hydrate (>80%), 3-chlorobenzaldehyde, 2-bromobenzaldehyde, mercuric chloride, mercuric acetate, other metal salts, methanol, and acetonitrile were procured from the local market and were used without further purification. Also, DMSO-d_6 used in recording NMR spectra and rhodamine 6G were procured from commercial sources. The solutions of various pH values were freshly prepared prior to use, and the pH was maintained by varying the volume of 0.1 N HCl, 0.1 N NaOH, and 0.1 N acetic acid as needed.

A PerkinElmer 'Spectrum 400' FT-IR spectrophotometer was used to record FT-IR spectra of compounds. NMR spectra were recorded using either a Bruker 400 MHz NMR or a JEOL 500 MHz NMR spectrometer. Solution pH was measured using a Cole-Parmer pH meter (pH 700). A UV-vis spectrophotometer of Shimadzu (UV2550) was used to record all absorption spectra. A Horiba Jobin Yvon (Fluoromax 4) spectrophotometer was used to record all fluorescence emission spectra. A time-correlated single photon counting (TCSPC) setup (Edinburgh Instruments, Life Spec II, UK) was employed to record the fluorescence lifetime of solutions, wherein a diode laser (510 nm wavelength) was used as the excitation source. Signals were collected using a Hamamatsu MCP PMT (3809U) detector. The UV-vis, fluorescence, and lifetime spectroscopic data were collected using a high-precision cell made of Quartz SUPRASIL (Hellma Analytics), with a 1 cm path length.

Experimental section

Synthesis, characterization, theoretical details, and other data mentioned in the manuscript are provided in the SI.

For titrations, 50 mL 10^{-5} M **EY-S$_O$** solution was prepared using ethanol–tris buffer (1 : 1, v/v), maintaining the pH at 7.2. 50 mL 10^{-4} M Hg^{2+} salt solution was prepared using tripledistilled water as the solvent. Similarly, titrations were also performed using **EY-S$_M$**.

The average lifetime of the sample was evaluated using eqn (1) (using fitting parameters for the tri-exponential function, $n = 3$).

$$\tau_{\text{avg}} = \frac{\sum_{i=1}^{n} B_i \tau_i^2}{\sum_{i=1}^{n} B_i \tau_i} \qquad (1)$$

A modified B–H (Benesi–Hildebrand) equation for 1 : 1 complexation was employed to determine the association constant (K_a) between **EY-S$_O$** (or **EY-S$_M$**) and Hg^{2+} ions (eqn (2)).[66,67]

$$\frac{\Delta I_{\max}}{\Delta I} = 1 + \frac{1}{K_a[\mathrm{Hg}^{2+}]} \qquad (2)$$

Quantum yields (ϕ) of the fluorescent samples were determined using a basic solution of fluorescein as a reference and employing eqn (3).[68]

$$\phi_{\text{sample}} = \frac{\phi_{\text{reference}} \times F_{\text{sample}} \times f_{\text{reference}} \times \eta_{\text{sample}}{}^2}{F_{\text{reference}} \times f_{\text{sample}} \times \eta_{\text{reference}}{}^2}. \qquad (3)$$

Herein, F is the area under the emission curve, f is the absorption factor ($f = 1\text{–}10^{-A}$ and A = absorbance), and η is the refractive index of the solvent.

The limit of detection (LOD) and limit of quantification (LOQ) were determined using eqn (4) and (5), respectively.[69–72]

$$\mathrm{LOD} = \frac{3\sigma}{K}. \qquad (4)$$

$$\mathrm{LOQ} = \frac{10\sigma}{K}. \qquad (5)$$

Here, σ is the standard deviation of five consecutive fluorescence data points of **EY-S$_O$** and K is the slope of the titration plot of fluorescence intensity *versus* $[Hg^{2+}]$.

Cell culture

Human breast adenocarcinoma (MDA-MB-231), human lung carcinoma (A-549), and human embryonic kidney (HEK-293) cells were obtained from the National Centre for Cell Science (NCCS, Pune, India). The MDA-MB-231, A-549, and HEK-293 lines were maintained in Dulbecco's modified Eagle medium (DMEM). All media were supplemented with 10% (v/v) heat-inactivated fetal bovine serum, 100 U mL^{-1} penicillin, and 100 μg mL^{-1} streptomycin. Cultures were kept in a humidified incubator at 37 °C and 5% CO_2 and sub-cultured at 70–80% confluence using 0.25% trypsin–EDTA. Stock solutions of the final test compounds were prepared in dimethyl sulfoxide (DMSO) at a concentration of 5 mM and stored at 4 °C until use in biological assays. Reagents used for ROS assay, including DCFH-DA, as well as those employed in live dead assay, such as calcein–AM blue and propidium iodide (PI), were procured from Sigma-Aldrich (USA). The assessment of apoptotic cell population was carried out using an Annexin V-FITC/PI dual staining kit (TACs, BioLegend, USA) in accordance with the manufacturer's guidelines.

MTT cell-viability assay

Cell viability after compound treatment was quantified by the MTT reduction method. Cells were seeded at 10×10^3 cells per well in 96-well plates and allowed to adhere overnight. Serial dilutions of the test samples (0.39 to 50 μM) in complete medium were added, and incubation continued for 48 h. After treatment, the spent media were aspirated, and 50 μL of the MTT solution (5 mg per mL in PBS) was added to each well, and the plates were returned to the incubator for 4 h. Purple formazan crystals were dissolved in 100 μL of dimethyl–sulfoxide with gentle shaking for 10 min. Absorbance was read at 570 nm (reference 650 nm) on a microplate reader. The percentage cell viability was calculated relative to untreated controls, and IC_{50} values were obtained from non-linear regression fits of dose–response curves using GraphPad Prism (version 8.0.1).[73–78]

Intracellular ROS assay

Reactive oxygen species generation was evaluated using the cell-permeable probe 2′,7′-dichlorofluorescin diacetate (DCFH-DA). MDA-MB-231 Cells were seeded on 12 mm coverslips in 12-well plates (5×10^4 cells per well) and incubated overnight for attachment.[79] Later, treated with the test compound **EY-M$_M$** and reference compound **BG-45** at their IC_{50} concentrations, or with complete medium 1% DMSO as a control, for 48 h. After the treatment period, the cells were gently washed with PBS and incubated with 10 μM DCFH-DA in PBS for 30 min in the dark at 37 °C. After two PBS washes, the cells were mounted on glass slides and imaged under a confocal microscope equipped with 480 nm and 535 nm filters. The images were then analyzed using ImageJ v1.54g to calculate the emitted fluorescence.[78]

Live/dead dual-fluorescence assay

To perform this study, MDA-MB-231 cells were seeded on 12 mm coverslips in 12-well plates (5×10^4 cells per well^{-1}) and incubated overnight for attachment.[80] Later, treated with the test compound **EY-M$_M$** and reference compound **BG-45** at their IC_{50} concentrations or with complete medium 1% DMSO as a control for 48 h. After a PBS rinse, cultures were incubated with 2 μM calcein–AM blue and 4 μM propidium iodide (PI) diluted in PBS for 30 min at 37 °C in the dark. Coverslips were washed twice, mounted on glass slides, and imaged immediately under a confocal microscope equipped with 480 nm and 535 nm filters.[81] Blue cells stained with calcein–AM blue were considered viable, whereas red-fluorescing cells stained with PI indicated compromised plasma membranes. The captured images were analysed using ImageJ v1.54g; the ratio of live to dead cells was expressed as a percentage relative fluorescence unit (RFU).[82]

Apoptosis detection by Annexin V-FITC/PI staining

Apoptotic cell death was assessed using a TACs/Annexin V assay kit (BioLegend, USA). MDA-MB-231 cells were seeded into 12-well culture plates at a density of 5×10^4 cells per well and incubated overnight to promote adherence.[83] After this initial incubation, the cells were treated with the lead molecule

EY-M$_M$ and the reference compound **BG-45** at their respective IC$_{50}$ concentrations. Treatment was carried out for 48 hours under standard culture conditions. Following treatment, cells were trypsinized, washed gently with phosphate-buffered saline (PBS, pH 7.4), and resuspended in 100 µL of freshly prepared staining solution. This solution was composed of 10 µL of 10× binding buffer, 1 µL of Annexin V conjugated with fluorescein isothiocyanate (FITC), and 10 µL of propidium iodide (PI), with the remaining volume made up using double-distilled water. The staining was carried out in the dark at room temperature for 30 minutes. After incubation, the samples were subjected to flow cytometric analysis using a BD Aria III flow cytometer. A minimum of 10 000 cellular events were recorded per sample, and data were used to distinguish live, early apoptotic, late apoptotic, and necrotic populations based on Annexin V-FITC and PI fluorescence patterns.[73–78,82]

Results and discussion

The organic sensors (**EY-S$_O$** and **EY-S$_M$**) reported herein are xanthene derivatives and were obtained in two steps. The lactam derivative of Eosin Y (**1**) was synthesized using a previously reported protocol.[79] In the subsequent step, an appropriate halosubstituted benzaldehyde was added to an acetonitrile solution of **1**, and the reaction mixture was refluxed for 12 hours to yield either **EY-S$_O$** or **EY-S$_M$** as the final product (Scheme 1). The presence of an imine functional group in the obtained products (**EY-S$_O$** and **EY-S$_M$**) was confirmed from their corresponding IR spectra, which had a band centered at 1611 cm^{-1} (Fig. S1 and S2). Additionally, the bands centered at 3182 cm^{-1} and 1702 cm^{-1} in **EY-S$_O$** (Fig. S1) and at 3192 cm^{-1} and 1610 cm^{-1} in **EY-S$_M$** (Fig. S2) were assigned to the phenolic –OH and carbonyl (of the lactam) functional groups, respectively. The molecules **EY-S$_O$** and **EY-S$_M$** were also characterized by using NMR spectroscopy. Herein, the presence of imine groups was confirmed by the appearance of peaks at 8.94 and 8.93 ppm in the ^{1}H NMR spectra of **EY-S$_O$** and **EY-S$_M$**, respectively (Fig. S3 and S4). Moreover, in the ^{13}C{^{1}H} NMR spectrum, the signal due to the lactam carbonyl carbon appeared at 174 ppm in **EY-S$_O$** (Fig. S5) and at 175 ppm in **EY-S$_M$** (Fig. S6).

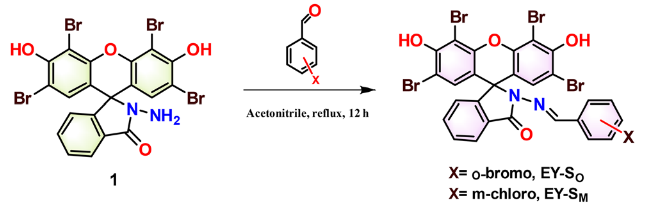

Scheme 1 Syntheses of **EY-S$_O$** and **EY-S$_M$**.

The metal-ion sensing capabilities of the newly synthesized molecules (**EY-S$_O$** and **EY-S$_M$**) were evaluated against a range of mono-, di-, and trivalent metal cations using UV-vis (Fig. 1) and fluorescence spectroscopy (Fig. 2). In an ethanol–tris buffer system (1 : 1, pH 7.2, 25 °C), both compounds (**EY-S$_O$** and **EY-S$_M$**) exhibited negligible absorbance within 400 to 800 nm and weak fluorescence emission at 534 nm and 551 nm upon excitation at 525 nm and 510 nm, respectively. These observations indicated the presence of a closed spirolactam conformation in the absence of metal ions. In the presence of environmentally relevant cations (K^+, Cu^+, Ag^+, Mn^{2+}, Fe^{2+}, Co^{2+}, Ni^{2+}, Cu^{2+}, Zn^{2+}, Hg^{2+}, Pb^{2+}, Al^{3+}, Cr^{3+}, and Fe^{3+}), only Hg^{2+} triggered marked optical shifts. The selective interaction of the synthesized molecules (**EY-S$_O$** and **EY-S$_M$**) in the presence of mercuric ions, as evident from the significant changes in the respective optical spectra, suggests the Hg^{2+}-induced spirolactam ring opening in these molecules. Consequently, fluorescence and vivid chromogenic changes were observed due to extended conjugation upon ring opening.

To further quantify the mercuric ion detection ability of **EY-S$_O$** and **EY-S$_M$**, UV-vis titrations were conducted by incremental addition of Hg^{2+} ion solution (10^{-4} M) to a sensor solution (10^{-5} M). **EY-S$_O$** and **EY-S$_M$** initially displayed a primary absorption band at 212 and 228 nm, accompanied by moderate

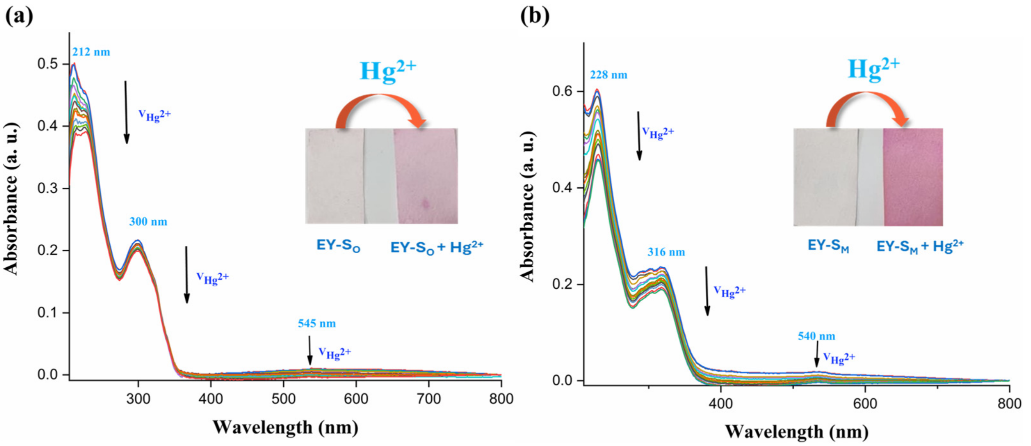

Fig. 1 UV-vis spectra (absorbance *vs.* wavelength) of a solution (10^{-5} M) of (a) **EY-S$_O$** and (b) **EY-S$_M$** and Hg^{2+} (10^{-4} M) in ethanol–tris buffer (1 : 1) at pH 7.2 and 25 °C; inset image in each plot shows the corresponding TLC strip experiment; left: TLC plate coated with the sensor and right: TLC plate coated with the sensor after exposure to Hg^{2+} ions.

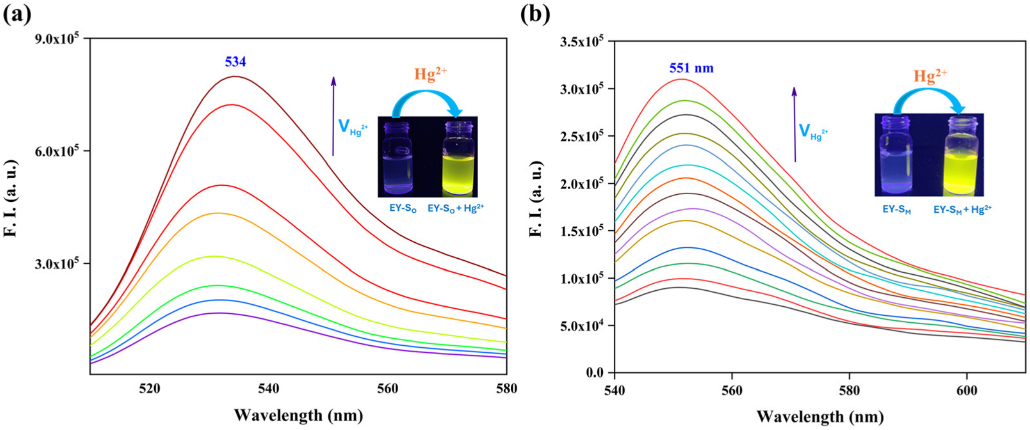

Fig. 2 Emission spectra (fluorescence intensity *vs.* wavelength) of a solution (10^{-5} M) of (a) **EY-S$_O$** and (b) **EY-S$_M$** and Hg^{2+} (10^{-4} M) in ethanol–tris buffer (1 : 1) at pH 7.2 and 25 °C. The inset image in each plot represents the corresponding visual experiment; left: a vial containing a methanolic solution of the sensor only and right: Hg^{2+} with a methanolic solution of the sensor.

absorptions at 300 and 316 nm and weaker absorptions at 545 and 540 nm, respectively. Progressive addition of Hg^{2+} led to a decrease in these signals until the addition of a 1 : 1 molar ratio of the analyte solution. These spectral transformations indicate 1 : 1 complexation and saturation of binding sites present in the probe molecules.

In order to evaluate the response of **EY-S$_O$** and **EY-S$_M$** towards Hg^{2+} ions, fluorescence titration studies were conducted under identical conditions as described for the UV-vis experiments. The molecule **EY-S$_O$** exhibited a fluorescence emission maximum at 534 nm (λ_{ex} = 525 nm). Initially weakly fluorescent, **EY-S$_O$** showed a ~4.8 fold increase in emission intensity upon addition of equimolar Hg^{2+} ions. No substantial increase in emission intensity was observed upon further addition of mercuric ions, indicating the saturation of binding sites within the host molecule (**EY-S$_O$**). The other sensor molecule (**EY-S$_M$**) displayed a similar turn-on response with an emission peak at 551 nm (λ_{ex} = 510 nm) and a ~3.5-fold increase in fluorescence emission intensity. The plots of fluorescence intensity (F.I.) *versus* Hg^{2+} ion concentration (Fig. S7 and S8), reveal excellent linearity (R^2 = 0.96) in **EY-S$_O$** and (R^2 = 0.99) in **EY-S$_M$** up to a 1 : 1 metal-to-sensor ratio. These results confirm that **EY-S$_O$** and **EY-S$_M$** are "turn-on" fluorescent probes for the selective detection of mercuric ions present in aqueous solutions. The fluorescence intensity ratio (F/F_0) exhibited a clear linear relationship with the analyte concentration (Hg^{2+} ions) across both low and high ranges (Fig. S9 and S10), indicating a static interaction mechanism for both sensors. This suggests that the mercuric ions form stable ground-state complexes with the sensors, rather than interacting through dynamic collisions. Overall, the compounds (**EY-S$_O$** and **EY-S$_M$**) respond consistently and predictably, making them reliable sensors for detecting aquated mercuric ions over a wide concentration range. This conclusion was further substantiated through fluorescence lifetime (τ) measurements. The lifetimes of both sensors were recorded in the presence of varying concentrations of Hg^{2+}, and calculated using eqn (1) (Fig. S11 and S12). The compiled data, presented in Table 1, revealed no appreciable change in fluorescence lifetimes upon addition of different concentrations of mercuric ions. This invariance of lifetime strongly supports a static interaction between the hosts (**EY-S$_O$** or **EY-S$_M$**) and the guest (Hg^{2+}), aligning with the conclusion drawn from the observed linearity of plots of F/F_0 *versus* [Hg^{2+}]. Thus, the molecular-level interaction involves the formation of a ground-state complex rather than a dynamic collisional complex.

Table 1 Lifetime-based titration data. Data represent the mean ± RSD (n = 3)

Sl. no.	Sensor 1	τ (ns)	Sensor 2	τ (ns)
1	**EY-S$_O$**	2.7 ± 2.8%	**EY-S$_M$**	3.3 ± 3.3%
2	**EY-S$_O$** + 25(%) Hg^{2+}	2.7 ± 2.9%	**EY-S$_M$** + 25(%) Hg^{2+}	3.3 ± 2.9%
3	**EY-S$_O$** + 50(%) Hg^{2+}	2.7 ± 2.4%	**EY-S$_M$** + 50(%) Hg^{2+}	3.3 ± 3.4%
4	**EY-S$_O$** + 75(%) Hg^{2+}	2.7 ± 2.6%	**EY-S$_M$** + 75(%) Hg^{2+}	3.3 ± 2.7%
5	**EY-S$_O$** + 100(%) Hg^{2+}	2.8 ± 3.3%	**EY-S$_M$** + 100(%) Hg^{2+}	3.3 ± 3.1%

To confirm the 1 : 1 stoichiometric complexation between the sensors (**EY-S$_O$** or **EY-S$_M$**) and Hg^{2+}, Job's method of continuous variation was employed.[72,84] Equimolar stock solutions in ethanol–water were mixed in varying ratios of each sensor and Hg^{2+}, keeping the total volume constant. Emission intensities were measured, and $\Delta I \times$ mole fraction of Hg^{2+} was plotted against the Hg^{2+} mole fraction. The maxima of each curve (Fig. S13 and S14) appeared at around 0.5 on the x-axis, which indicated the formation of a 1 : 1 complex due to sensor-Hg^{2+} interactions.

Based on the confirmation of 1 : 1 complexation as evident from the Job's plot, the association constants between each sensor and Hg^{2+} were elucidated *via* the modified Benesi–Hildebrand (B–H) plot (Fig. 3 and Fig. S15) using eqn (2). From the linear fitting values of the respective plots, the binding strengths were estimated (with mean ± SD, n = 3) as $3.25 \times 10^4 \pm 9.3 \times 10^2$ M^{-1} for **EY-S$_O$** and $1.08 \times 10^5 \pm 2.9 \times 10^3$ M^{-1} for **EY-S$_M$**. The values clearly indicate the high Hg^{2+} ion affinity of both sensors (**EY-S$_O$** and **EY-S$_M$**).

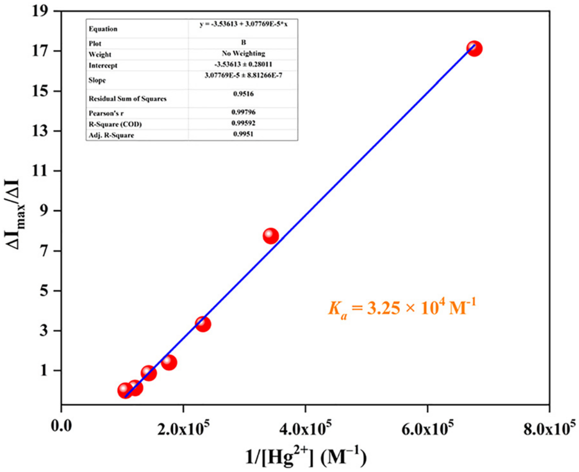

Fig. 3 B–H plot of **EY-S$_O$** based on fluorescence titration with aquated mercuric ions.

To assess the sensing capabilities of **EY-S$_O$** and **EY-S$_M$**, the limit of detection (LOD) and limit of quantification (LOQ) were calculated using eqn (4) and (5), and the data are presented in a tabular form in Table 2. Fluorescence measurements (Tables S1 and S2) were recorded at intervals of two minutes during titrations, and slopes were measured from the plots of F.I. *vs.* [Hg^{2+}] (Fig. S7 and S8). The resulting nanomolar LOD and LOQ values emphasize that **EY-S$_O$** and **EY-S$_M$** are highly sensitive towards the detection of Hg^{2+} ions present in aqueous media. These results also highlight their potential to detect Hg^{2+} ions present in ultra-trace concentration levels. The LOD data of **EY-S$_O$** and **EY-S$_M$** were compared with those of other reported sensors used for sensing Hg^{2+} (Table S3).

The quantum yields (ϕ) of **EY-S$_O$**, **EY-S$_M$**, and their complexes with Hg^{2+} ions (**EY-M$_O$** and **EY-M$_M$**) were estimated using rhodamine 6G (ethanol solution) as the reference, having ϕ_{ref} = 0.95. The experimental data revealed that the quantum yield of the sensors increased significantly upon complex formation with mercuric ions (Table 3). This pronounced amplification in fluorescence emission upon Hg^{2+} coordination enriches the literature of mercury ion detection with "turn-on" mechanisms, of which there are only a very few examples.

To evaluate the selectivity of sensors (**EY-S$_O$** and **EY-S$_M$**) toward Hg^{2+} ions, their performance was tested in the presence of various mono-, di-, and trivalent metal ions (K^+, Cu^+, Ag^+, Fe^{2+}, Mn^{2+}, Co^{2+}, Ni^{2+}, Cu^{2+}, Zn^{2+}, Pb^{2+}, Al^{3+}, Cr^{3+}, and Fe^{3+}). In these experiments, cation complexation by the sensors was tested by adding an excess of another cation (five equivalents) in ethanolic sensor solutions. None of the other cations exhibited notable binding, as depicted in Fig. 4a, suggesting that the ionic radius of Hg^{2+} aligns optimally with the cavity created upon opening of the spiro-lactam ring in both the sensor molecules. Further competitive experiments involving **EY-S$_O$** and **EY-S$_M$** confirmed this selectivity. While the fluorescence intensity of the sensor remained unaffected in the presence of an excess of another cation, a significant turn-on response was observed in the fluorescence emission of the sensor upon addition of Hg^{2+} ions in **EY-S$_O$** (Fig. 4a and Table S4, Fig. S27, S28). A similar trend was also observed for **EY-S$_M$** (Fig. S16 and Fig. S29, S30, Table S5). These observations again suggest the efficiency of the sensors for Hg^{2+} detection in the presence of other competing ions and prompt their possible application as selective mercury sensors for practical purposes.

Table 2 LOD and LOQ for **EY-S$_O$** and **EY-S$_M$**. Data represent the mean ± SD (n = 3)

Sl. no.	Sensor	LOD (nM)	LOQ (nM)
1	**EY-S$_O$**	6.01 ± 0.57	20.04 ± 0.19
2	**EY-S$_M$**	5.93 ± 0.09	19.76 ± 0.03

Table 3 Quantum yield of sensors and their corresponding Hg^{2+} complexes. Data represent the mean ± RSD (n = 3)

Sl. no.	Compound	Quantum yield (ϕ)
1	**EY-S$_O$**	0.19 ± 3.2%
2	**EY-S$_M$**	0.11 ± 2.4%
3	**EY-M$_O$**	0.58 ± 3.1%
4	**EY-M$_M$**	0.51 ± 3.5%

We were also curious to study the Hg^{2+} sensing performance of sensors at various pH levels. Thus, the influence of pH (1–10) on mercuric ion detection was systematically investigated by incremental addition of Hg^{2+} ions (1 : 1 molar ratio) at each pH condition. Fluorescence measurements revealed a pronounced pH-dependent response. In highly acidic solutions (pH = 1–3), the fluorescence emission enhancement upon Hg^{2+} addition was negligible, suggesting poor sensing efficiency in this pH range. Moderate improvement was observed at pH 4–5, though the response remained suboptimal. In contrast, a significant increase in fluorescence intensity was recorded when the pH of the solution was between pH 6 and 9, and maximum emission enhancement was recorded at pH 7. Beyond pH 9, the sensing ability declined progressively. A similar trend was also observed for **EY-S$_M$**. This pH-dependent sensing behavior is attributed to the pH-dependent deprotonation of the phenolic –OH groups in the sensors. Under acidic conditions (pH ≤ 5), deprotonation is restricted, and consequently, the spirolactam ring remains closed. Hence, at pH ≤ 5, the non-fluorescent form predominates, and this limits Hg^{2+} complexation by the sensors to a considerable extent. As pH increases from 6 to 9, facile deprotonation of the phenolic –OH groups promotes ring opening and the facile formation of the fluorescent mercury(II) complexes of the sensors. However, at alkaline pH (≥9), Hg^{2+} preferentially binds to hydroxide ions (present in higher concentrations), thereby reducing the interaction of mercuric ions with sensors and diminishing fluorescence emission output.[85]

The sustainable use of **EY-S$_O$** and **EY-S$_M$** was demonstrated through their recyclability in Hg^{2+} detection events. Sulphide (S^{2-}) ions effectively displaced sensor-bound Hg^{2+}, regenerating ~90% of each sensor for reuse.[86] The probe could be regenerated up to five cycles with negligible losses in sensing efficacy, as evidenced by a consistent emission intensity

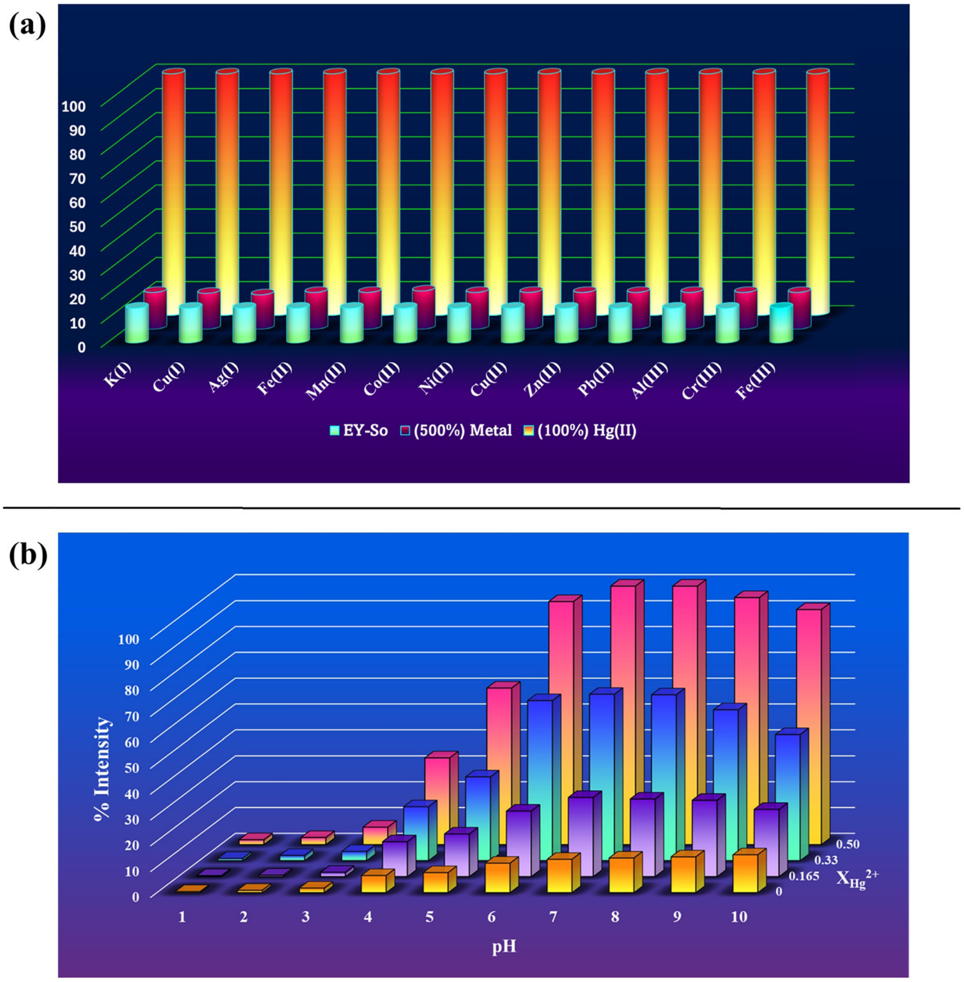

Fig. 4 (a) Interaction of **EY-So** with other metals and the effect of interference of other metals and the (b) effect of pH variation (1–10, at 1 pH interval) on the sensing of Hg^{2+} by **EY-So**.

(Fig. S17 and S18). Unlike typical dye-based probes that degrade upon Hg^{2+} binding, **EY-S$_O$** and **EY-S$_M$** maintained structural integrity throughout the sensing event. Functioning as reversible chelating ligands, the sensors (**EY-S$_O$** and **EY-S$_M$**) bind Hg^{2+} and return to their native form post-decomplexation, exemplifying their durability and cost-effectiveness.

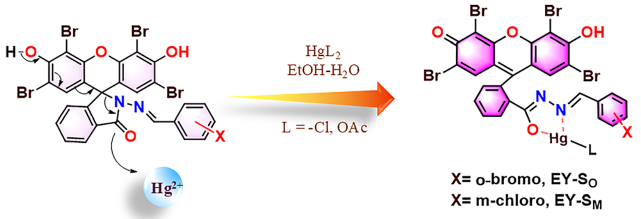

Scheme 2 Mechanism of **EY-S$_O$** and **EY-S$_M$**.

Mechanism of binding of sensors (EY-S$_O$ and EY-S$_M$) with mercuric ions

Formation of 1 : 1 host–guest complexes between Hg^{2+} ions and sensors **EY-S$_O$** and **EY-S$_M$** was confirmed *via* multiple analytical techniques. The resulting metallacycles, **EY-M$_O$** and **EY-M$_M$** (Scheme 2), indicate the chelating nature of these sensors. Complexation initiates with the opening of the spirolactam ring, which is facilitated by the fluorescein-like framework and subsequently enables the Hg^{2+} ion coordination *via* the hydrazide (N) and spirolactam (O) centers. This interaction leads to the formation of an optimal five-membered ring in the metallated sensor designated as **EY-M$_O$** and **EY-M$_M$** *via* the creation of selective binding pockets for Hg^{2+}. Concurrently, the tautomer formed has an extended π-conjugation, due to which the visual color/fluorescence shifts are observed. The evidence for the formation of **EY-M$_O$** and **EY-M$_M$** (Scheme 2) was obtained from FT-IR and NMR data. In **EY-M$_O$**, intensities of imine and lactam carbonyl stretches at 1611 and 1702 cm^{-1} decreased significantly (Fig. S19 and S20), which confirmed the chelation of the sensors with Hg^{2+}.

Additionally, upon complexation, a slight upfield shift of proton signals was observed in the ^1H NMR spectrum, moving from 8.93 ppm of imine in **EY–S$_O$** to 8.89 ppm in **EY–Mo** (Fig. S3 and S21). A similar shift in peaks was observed for **EY–M$_M$** also

(Fig. S22). Also, the $^{13}C\{^1H\}$ NMR spectra of the metal complexes (Fig. S23 and S24) were different from those of the sensors. During NMR titration, peaks due to hydrogens present in other functional groups (like imine and aromatic rings) remained unchanged. These observations accounted for the proposed complexation between the sensors (**EY-S$_O$** and **EY-S$_M$**) and the analyte (Hg^{2+} ions) and also simultaneously ruled out the possibility of **EY-S$_O$** and **EY-S$_M$** acting as a chemodosimeter.

Furthermore, we have explored the ^1H NMR titration of **EY-S$_O$** *vs.* Hg^{2+} as peaks of –OH were clearly visible in the case of **EY-S$_O$**. The ^1H NMR spectrum of **EY-S$_O$** was recorded upon the gradual addition of $Hg(OAc)_2$ (Hg^{2+} ions) (Fig. 5 and Fig. S31–S36). With the addition of 0.20, 0.40, 0.60, and 0.80 equivalents of Hg^{2+}, the intensities of the signal corresponding to the –OH proton progressively decreased (Fig. S32–S35). Upon addition of 1.0 equivalent of Hg^{2+}, these signals almost completely disappeared (Fig. S36). In contrast, the signals corresponding to protons of other functional groups, such as the imine and aromatic moieties, remained essentially unchanged during the titration. These results support the proposed complexation between the sensor (**EY-S$_O$**) and Hg^{2+} ions, while simultaneously ruling out the possibility of **EY-S$_O$** functioning as a chemodosimeter.

The solid-state sensing capabilities of the probes **EY-S$_O$** and **EY-S$_M$** were evaluated using a thin-layer chromatography (TLC) strip-based assay. The TLC plates were initially immersed in methanolic solutions (10^{-4} M) of the respective sensors (**EY-S$_O$** or **EY-S$_M$**), followed by air-drying to ensure uniform coating. Subsequently, the pale pink coloured sensor-coated plates were exposed to aqueous mercury(II) ion solutions (10^{-3} M). Both **EY-S$_O$** and **EY-S$_M$** coated plates exhibited an instant and distinct colour change from faint pink to magenta (insets in Fig. 1a and b), thereby confirming their rapid and effective solid-state response to Hg^{2+} ions.

To demonstrate the practical application of **EY-S$_O$** and **EY-S$_M$** as molecular sensors, a smartphone-assisted fluorescence sensing system was successfully developed for Hg^{2+} detection by both sensors. The objective was to replace conventional, cumbersome, and expensive instrumentation with a compact, image-based approach (Fig. 6) using a smartphone, of which there are more than four billion global users. The chromogenic changes associated with the detection of mercuric ions were visible through the unaided vision (naked eye). However, for rapid detection (both qualitative and quantitative) of mercuric ions without the use of a spectrophotometer, the image processing technique using a smartphone appears more convenient. This strategy is based on the RGB (Red–Green–Blue) model, where the RGB values corresponding to the perceived colour are estimated. It is well-known that a white colour corresponds to 255, 255, 255 as the R, G, B values respectively, while a black colour has R, G, B values equal to 0, 0, 0, respectively. In our experiments, solutions of the sensor (**EY-S$_O$** or **EY-S$_M$**) having a concentration of 1×10^{-4} M were treated with solutions of mercuric ions of concentrations up to 120 μM, which resulted in fluorescence enhancements, as anticipated. Fluorescence images of these real-time sample solutions were captured under UV illumination (using a UV torch) using the rear camera of an Android-based smartphone (One Plus Nord 5G). Finally, the images obtained were processed *via* two analytical routes, namely (a) ImageJ based RGB channel analysis in which among

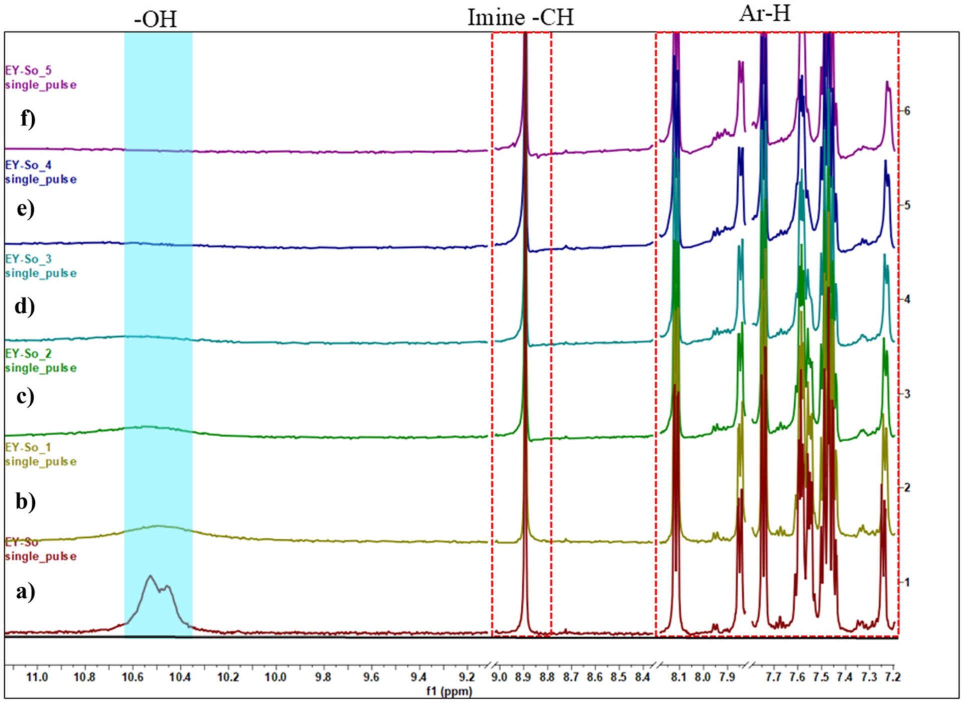

Fig. 5 Stacked ^1H NMR titration of Hg^{2+} sensing by **EY-S$_O$** (recorded in DMSO-d$_6$). (a) Only **EY-S$_O$**, (b) **EY-S$_O$** and 0.20 equivalents of Hg^{2+}, (c) **EY-S$_O$** and 0.40 equivalents of Hg^{2+}, (d) **EY-S$_O$** and 0.60 equivalents of Hg^{2+}, (e) **EY-S$_O$** and 0.80 equivalents of Hg^{2+}, and (f) **EY-S$_O$** and 1 equivalent of Hg^{2+}.

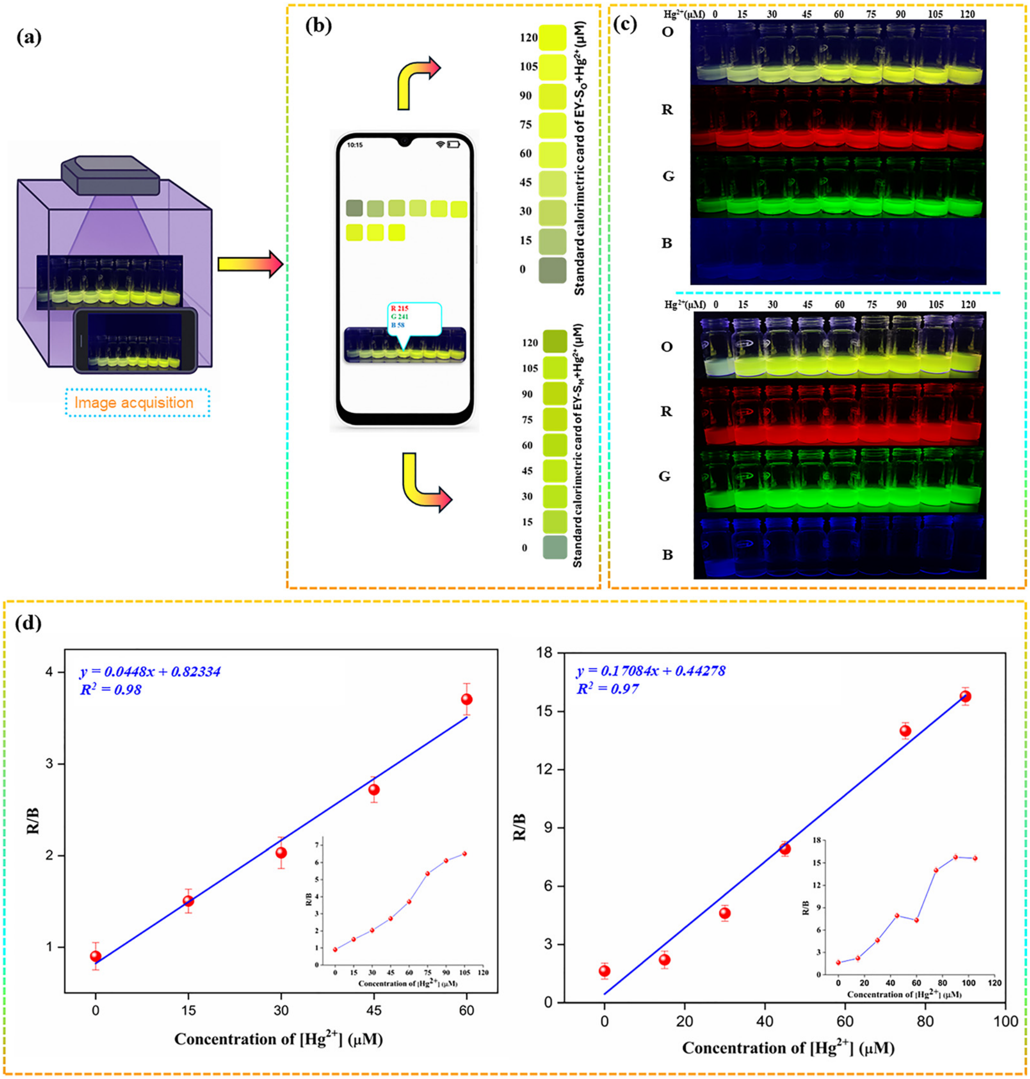

Fig. 6 (a) Image acquisition, (b) RGB analysis result of sensors using mobile application and an output colorimetric card for **EY-S$_O$** (top) and **EY-S$_M$** (down), (c) relationship between the Hg^{2+} concentration (0–120 μM) and R, G, B channel using ImageJ software, and the (d) relationship between R/B *vs.* concentration of Hg^{2+} (0–120 μM) using ImageJ for **EY-S$_O$** (top) and **EY-S$_M$** (down) (inset: R/B *vs.* concentration of [Hg^{2+}]) (O = original, R = red, G = green, and B = blue).

the various possible combinations, the plot of R/B ratio *vs.* change in the concentration of mercuric ions yielded linear calibration curves for **EY-S$_O$** and **EY-S$_M$** with $y = 0.0448x + 0.82334$, ($R^2 = 0.98$) and $y = 0.1784x + 0.44278$, ($R2 = 0.97$) and (b) native smartphone software (a color picker Application available in Google Play store) which showed linear relation of R with Hg^{2+} concentration for **EY-S$_O$** and **EY-S$_M$** (Fig. S25 and S26). These results obtained from image analysis closely matched those from traditional fluorescence spectroscopy, which confirmed the analytical reliability of this protocol and also demonstrated its strong potential for rapid, convenient, economic, precise, and on-site monitoring of nanomolar concentrations of mercuric ions for environmental remediation applications.

The complexes **EY-M$_O$** and **EY-M$_M$** exhibited significantly enhanced fluorescence relative to their unmetallated analogues **EY-S$_O$** and **EY-S$_M$** that prompted us to further investigate their potential biological activity. It is well-documented in the recent literature that fluorescent species can facilitate the generation of reactive oxygen species (ROS) in solution—a phenomenon that is closely linked to oxidative stress-mediated cytotoxicity in malignant cells. Recognizing the therapeutic implications of ROS induction, we extended our study to evaluate the anti-cancer efficacy of these emissive complexes (**EY-M$_O$** and **EY-M$_M$**). Therefore, we explored their cytotoxicity against two cancer cell lines as well as a healthy cell line in order to validate their potential as dual-function agents—serving both as luminescent probes and as candidates for targeted cancer therapy.

MTT assay

The synthesized sensors **EY-S$_O$** and **EY-S$_M$** and their corresponding metallacycles **EY-M$_O$** and **EY-M$_M$** were evaluated for

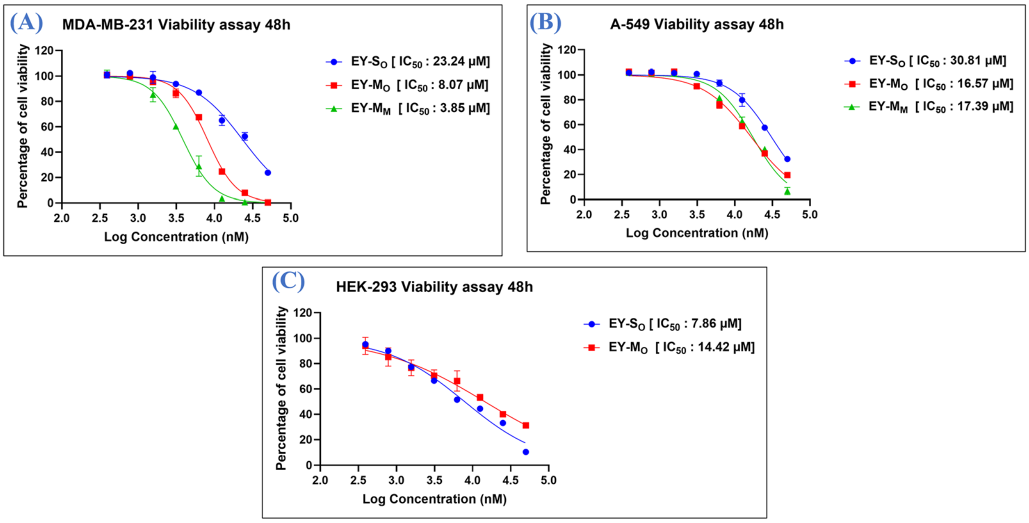

Fig. 7 Cytotoxicity study of the sensors **EY-S$_O$** and **EY-S$_M$** and their Hg^{2+} complexes **EY-M$_O$** and **EY-M$_M$** obtained by the MTT assay for 48 h in (A) MDA-MB-231, (B) A-549, and (C) HEK-293 cell lines. In this study, the cultured cells were treated with compounds in the concentration range of 0.39 to 50 µM (n = 2) for 48 h. The graphs were plotted using GraphPad Prism version 8.0.1. Data represent the mean ± SD (n = 2).

their *in vitro* cytotoxicity against human cancer cell lines MDA-MB-231 (triple-negative breast cancer) and A-549 (lung adenocarcinoma), with HEK-293 (human embryonic kidney) cells used as a normal control to assess selectivity.[87] The corresponding dose–response curves are shown in Fig. 7, and the results are summarized in Table 4. Among the ligands, **EY-S$_O$** exhibited moderate cytotoxic activity in both MDA-MB-231 and A-549 cell lines, while **EY-S$_M$** showed negligible cytotoxicity across the tested concentration range. Notably, a significant enhancement in cytotoxic potential was observed upon complexation with mercury. The Hg-complex **EY-M$_M$** displayed potent anticancer activity, particularly in MDA-MB-231 cells, with an IC$_{50}$ value of 3.85 µM. Furthermore, **EY-M$_M$** demonstrated minimal toxicity toward HEK-293 cells within the same concentration range, resulting in a selectivity index of more than 13-fold, indicating strong preferential activity toward cancer cells. In contrast, **EY-M$_O$** showed moderate cytotoxicity in both cancer cell lines but also affected the viability of HEK-293 cells, with an IC$_{50}$ value of 14.42 µM, suggesting limited selectivity. Furthermore, to ascertain that the observed cytotoxicity arises from the Hg-sensor complexes rather than from free mercuric ions, HgCl$_2$ was evaluated under identical experimental conditions. Notably, HgCl$_2$ did not exhibit much cytotoxicity up to a concentration of 50 µM in the tested cell lines [Fig. S37]. This observation confirms that the biological effects observed are intrinsic to the formed metallocyclic complexes and are not significantly attributed to the presence of free Hg^{2+} ions alone. These findings highlight **EY-M$_M$** as a promising lead candidate with potent and selective anticancer properties, whereas **EY-M$_O$** and the uncomplexed ligands exhibit less favorable therapeutic profiles.

Table 4 IC$_{50}$ (µM) values of the ligand and Hg-ligand complexes obtained by the MTT assay in MDA-MB-231, A-549 and HEK-293 cell lines. Data represent the mean ± SD (n = 2)

Compound	MDA-MB-231 IC$_{50}$ (µM)	A-549 IC$_{50}$ (µM)	HEK-293 IC$_{50}$ (µM)	Selectivity index (for MDA-MB-231)
EY-S$_O$	23.24 ± 2.31	30.81 ± 2.14	7.86 ± 1.15	0.34
EY-M$_O$	8.07 ± 0.43	16.57 ± 1.48	14.42 ± 2.77	1.79
EY-S$_M$	> 50	> 50	> 50	—
EY-M$_M$	3.85 ± 0.306	17.39 ± 1.85	> 50	12.99
BG-45	41.80 ± 0.25	29.14 ± 2.79	145.85 ± 0.19	3.49
HgCl$_2$	≫50	≫50	≫50	—

ROS assay

Detection of intracellular reactive oxygen species (ROS) is a critical approach for assessing oxidative stress, a key factor involved in various cellular processes, including apoptosis, mitochondrial dysfunction, and drug-induced cytotoxicity. Among the widely used probes for ROS detection, 2′,7′-dichlorodihydrofluorescein diacetate (DCFH-DA) is a well-established, cell-permeable fluorescent dye that enables visualization and quantification of ROS levels in live cells. Once inside the cell, DCFH-DA is deacetylated by intracellular esterases to non-fluorescent DCFH, which is then oxidized by ROS, such as hydrogen peroxide, hydroxyl radicals, and peroxynitrite, into highly fluorescent 2′,7′-dichlorofluorescein (DCF). This oxidation-dependent fluorescence serves as a reliable indicator of overall ROS activity. Under fluorescence microscopy, ROS-positive cells exhibit bright green cytoplasmic fluorescence, with an intensity proportional to the amount of ROS generated. In contrast, cells with low ROS levels display minimal or no fluorescence. This staining technique enables the sensitive detection of drug-induced oxidative stress, as well as real-time assessment of redox homeostasis within cells. In this study, DCFH-DA staining was employed to evaluate ROS generation in MDA-MB-231 cells following treatment with the test compound **EY-M$_M$** and reference compound **BG-45**. Fig. 8 illustrates the results of ROS induced by the treatment of the test compound **EY-M$_M$** and **BG-45** as the reference compound. The green fluorescence intensity

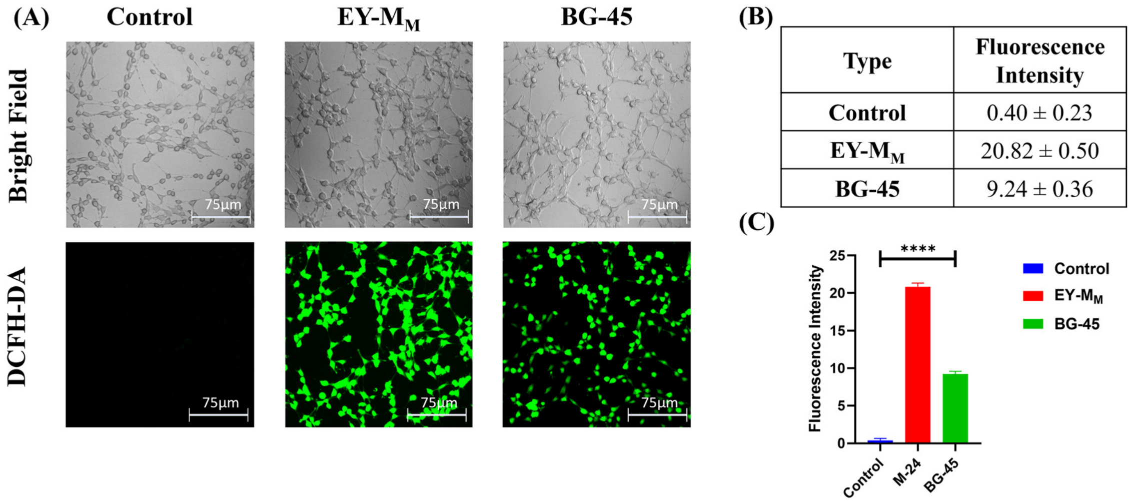

Type	Fluorescence Intensity
Control	0.40 ± 0.23
EY-M_M	20.82 ± 0.50
BG-45	9.24 ± 0.36

Fig. 8 Assessment of reactive oxygen species (ROS) levels within cells *via* DCFH-DA. (A) Representative confocal images of MDA-MB-231 cells stained with the ROS-sensitive dye DCFH-DA after treatment. (B) Tabulated data showing the quantitative analysis of fluorescence intensity, evaluated using ImageJ software. (C) Graphical representation of the quantified fluorescence intensity values derived using ImageJ analysis. Imaging was performed using a Leica DMI8 laser scanning confocal microscope (Leica Microsystems, Germany) at 20× magnification. Scale bar: 75 µm. Data are expressed as the mean ± standard deviation (n = 3); **** $p < 0.0001$ indicates statistical significance.

observed in treated cells directly correlates with the extent of ROS production, providing mechanistic insights into the oxidative stress-mediated cytotoxic effects of the tested compounds.

Live/dead dual-fluorescence assay

Live/dead cell staining is a widely adopted technique for evaluating cell viability, membrane integrity, and cytotoxic responses to various treatments. Calcein–AM blue and propidium iodide (PI) are the commonly used fluorescent dyes for the dual-labeling of live and dead cells, respectively. Calcein–AM blue is a cell-permeable, non-fluorescent ester that is converted by intracellular esterases into a blue-fluorescent calcein derivative in viable cells. This fluorescence marks the presence of active metabolism and intact plasma membranes. In contrast, PI is a membrane-impermeant nucleic acid stain that selectively penetrates cells with compromised membranes, typically dead or late-stage apoptotic cells, binding to DNA and fluorescing red upon intercalation. Under fluorescence microscopy, live cells appear

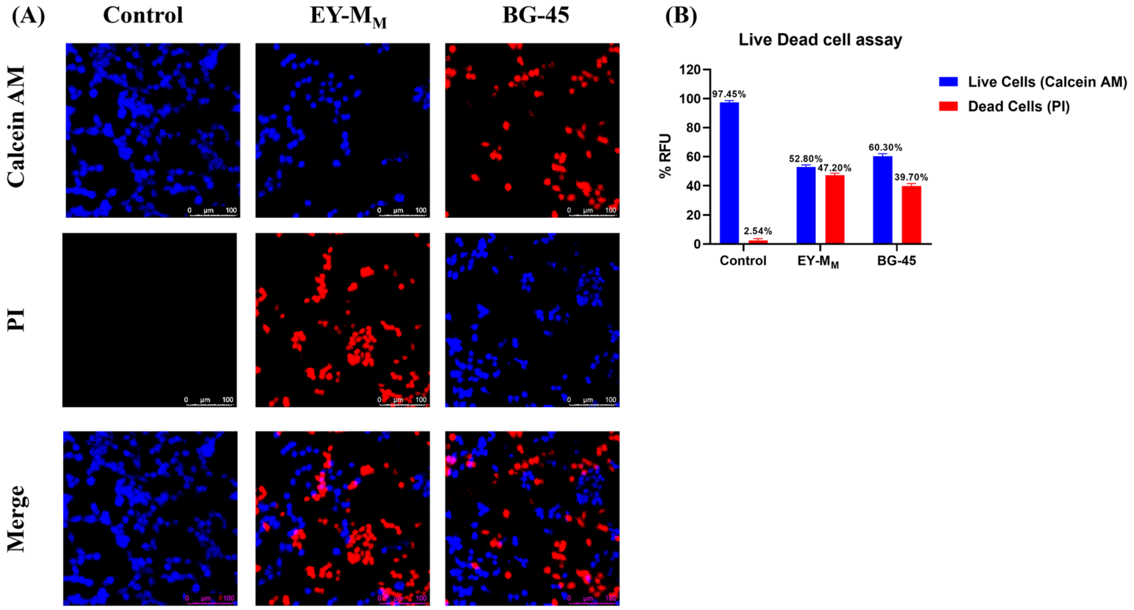

Fig. 9 (A) Representative confocal microscopy images of MDA-MB-231 cells stained with calcein–AM (blue, viable cells) and propidium iodide (PI, red, dead cells) following treatment. (B) Quantitative analysis of the fluorescence intensity was performed using ImageJ, showing the proportion of live and dead cells. Imaging was conducted using a Leica DMI8 laser scanning confocal microscope (Leica Microsystems, Germany) at 20× magnification. Scale bar: 100 µm. Data are presented as the mean ± standard deviation (n = 3).

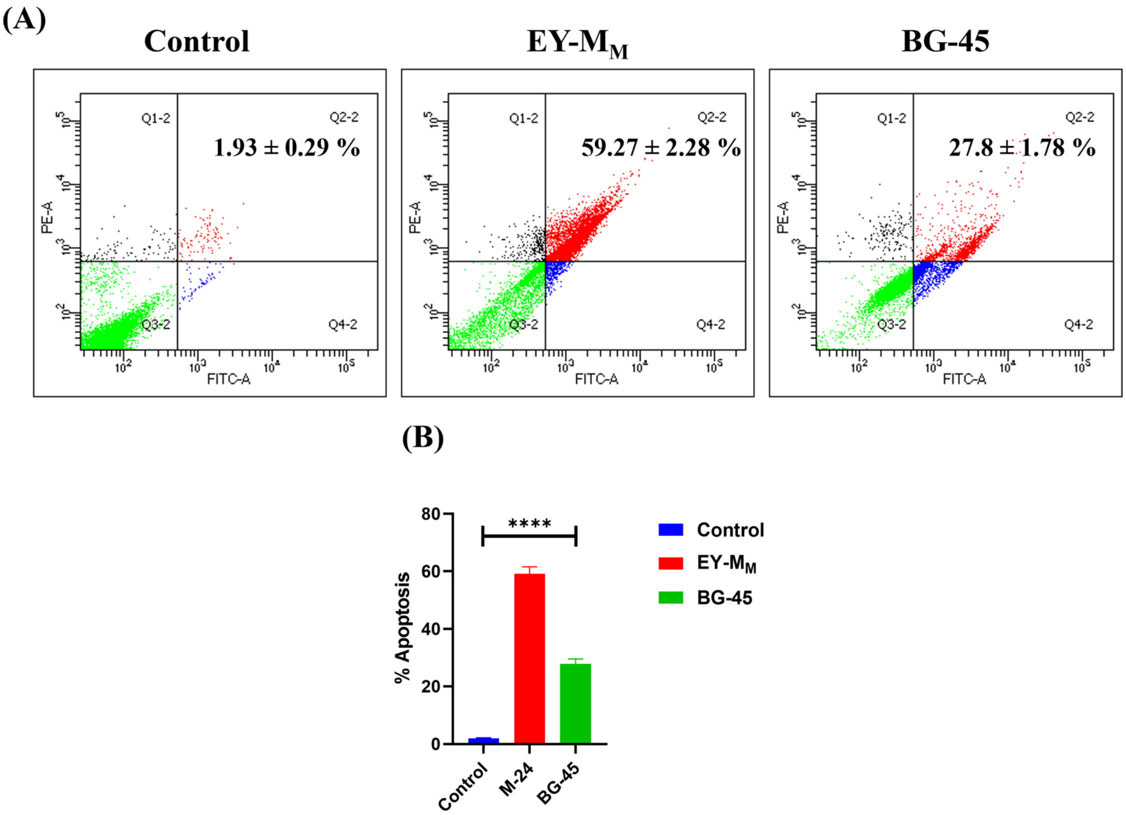

Fig. 10 (A) Flow cytometric analysis of apoptosis was conducted using Annexin-V and propidium iodide (PI) dual staining. MDA-MB-231 human breast cancer cells were treated for 48 hours with either 1% DMSO as a control, **EY-M$_M$** (3.85 μM), or **BG-45** (41.8 μM), corresponding to their respective IC$_{50}$ values determined by the MTT assay. The resulting dot plots delineate four distinct cell populations: necrotic (Q1), late apoptotic (Q2), viable (Q3), and early apoptotic (Q4) cells. (B) Bar graphs illustrating the cumulative percentage of apoptotic cells (sum of early and late apoptotic populations) post-treatment, highlighting the pro-apoptotic effects of **EY-M$_M$** and **BG-45** compared to the control group.

bright blue, while dead cells fluoresce red, allowing for a clear, binary distinction between viable and non-viable populations. This assay is especially useful in assessing the cytotoxicity profile of test compounds and for visualizing treatment-induced cell death. In the present study, MDA-MB-231 cells were subjected to live/dead staining following treatment with the lead compound **EY-M$_M$** and the reference compound **BG-45** to assess their effect on cell viability. Fig. 9 illustrates the results of live and dead cells with the treatment of the test compound **EY-M$_M$** and **BG-45** as the reference compound. A distinct increase in PI-positive (red) cells, accompanied by a reduction in calcein AM-positive (blue) cells, was observed upon **EY-M$_M$** treatment, indicating a loss of membrane integrity and significant induction of cell death. These results highlight the potent cytotoxic effect of **EY-M$_M$**, consistent with its activity in complementary assays such as ROS generation and nuclear fragmentation studies.

Apoptosis assay

The *in vitro* cytotoxicity studies demonstrated that the novel Hg-based complex **EY-M$_M$** exhibited potent anticancer activity against MDA-MB-231 breast cancer cells. To further investigate the mechanism of cell death, apoptosis assays were conducted in MDA-MB-231 cells using the test compound **EY-M$_M$** and the reference compound **BG-45** at their respective IC$_{50}$ concentrations.

In the Annexin V-FITC/PI dual-staining assay, an increase in Annexin V-positive, PI-negative cells corresponds to early apoptosis, whereas dual Annexin V- and PI-positive staining indicates late apoptosis. The *X*-axis and *Y*-axis represent fluorescence intensities of Annexin V and PI, respectively. Following treatment, the total percentage of apoptotic cells (early and late apoptosis combined) increased significantly from 1.93% in the untreated control group to 59.27% in the **EY-M$_M$**-treated group, indicating a robust induction of apoptosis. For comparison, cells treated with the reference compound **BG-45** exhibited a total apoptotic fraction of 27.8% under identical conditions. These findings clearly demonstrate that **EY-M$_M$** induces a significantly stronger apoptotic response compared to untreated cells, highlighting its potential as a promising anticancer agent (Fig. 10).

Conclusion

In summary, we developed two eosin Y-hydrazide and different benzaldehyde coupled organic chemosensors, **EY-S$_O$** and **EY-S$_M$**. Both molecules detected Hg^{2+} from water with high selectivity, sensitivity, and recyclability. No other metal ions interfered with Hg^{2+} ion sensing. UV-vis titration of both revealed colorimetric detection, and fluorescence titration revealed turn-on fluorescence during the course of detection. Job's plot ensured 1 : 1 binding, and the B–H plot displayed a high association constant of both **EY-S$_O$** and **EY-S$_M$** with Hg^{2+} ($3.25 \times 10^4 \pm 9.3 \times 10^2$ M^{-1} for **EY-S$_O$** and $1.08 \times 10^5 \pm 2.9 \times 10^3$ M^{-1} for **EY-S$_M$**), which facilitated the high sensitivity. The limits of detection and quantification are in the nM range for both sensors. Detection was the least in low pH and the most in neutral to slightly basic pH. Both sensors could be recycled at least five times using sulphide ions without much change in sensing performance in subsequent cycles. Based on the NMR and IR data, a plausible mechanism of binding was proposed. Moreover, a smartphone-based study of fluorescence was carried out to see the RGB analysis. The turn-on fluorescence motivated us to see the potential of sensors (**EY-S$_O$** and **EY-S$_M$**) and their corresponding Hg^{2+} complexes (**EY-M$_O$** and **EY-M$_M$**) against cancer cells (MDA-MB-231 and A-549) and normal cells (HEK-293). The IC$_{50}$ data revealed that both complexes showed superior anticancer activity than their Hg^{2+} detached unmetallated forms. Moreover, **EY-M$_O$** and **EY-M$_M$** were more effective against MDA-MB-231 than A-549, and both have appreciable selectivity against the HEK-293 cells. However, in terms of IC$_{50}$ and selectivity, **EY-M$_M$** delivered better anticancer activity than **EY-M$_O$**, which was further established by ample cell death mechanisms such as the ROS assay, live/dead dual-fluorescence assay, and Annexin V-FITC/PI dual-staining assay. While **EY-S$_O$** and **EY-S$_M$** exhibited comparable sensing performances in terms of selectivity, sensitivity, and recyclability, their respective mercury(II) complexes (**EY-M$_O$** and **EY-M$_M$**) displayed noticeably different anticancer activities. Overall, we converted toxic Hg^{2+} ions, detected in contaminated water, by two biocompatible sensors into potent anticancer agents.

Author contributions

All authors contributed equally to the manuscript. ND and BG supervised the project and edited the final version of the manuscript.

Conflicts of interest

Authors declare no competing financial or any other interest.

Data availability

Supporting data are available in the supplementary information (SI). Supplementary information: syntheses, characterization data, calculations, plots as mentioned in different sections, and other details. See DOI: https://doi.org/10.1039/d6ma00152a.

Acknowledgements

AC, BK, and AM acknowledge IIT Patna for their respective fellowships. VM acknowledges Student fellowships provided by the BITS-RMIT joint PhD program. ND acknowledges IIT Patna, and BG acknowledges the Birla Institute of Technology and Science, Pilani, Hyderabad Campus. The authors acknowledge SAIF, IIT Patna, for providing the NMR (500 MHz) data.

References

1 Y.-S. Wu, A. I. Osman, M. Hosny, A. M. Elgarahy, A. S. Eltaweil, D. W. Rooney, Z. Chen, N. S. Rahim, M. Sekar, S. C. B. Gopinath, N. N. I. Mat Rani, K. Batumalaie and P.-S. Yap, *ACS Omega*, 2024, **9**, 5100–5126.
2 M. Balali-Mood, K. Naseri, Z. Tahergorabi, M. R. Khazdair and M. Sadeghi, *Front. Pharmacol.*, 2021, **12**, 643972.
3 W. Ma, Q. Zhang, D. Xiang, K. Mao, J. Xue, Z. Chen, Z. Chen, W. Du, K. Zhai and H. Zhang, *Chem. – Eur. J.*, 2025, **31**, e202403760.
4 Z. W. Jiang, C. Yang, M. Wu, P. Zhang, Y. Liu, X. Gong and Y. Wang, *Microchem. J.*, 2025, **214**, 114088.
5 M. Saleem, M. Rafiq and M. Hanif, *J. Fluoresc.*, 2017, **27**, 31–58.
6 S. Chakraborty, K. Das and S. Halder, *Inorg. Chim. Acta*, 2024, **566**, 122026.
7 A. Thakuri, A. A. Bhosle, S. D. Hiremath, M. Banerjee and A. Chatterjee, *J. Hazard. Mater.*, 2024, **469**, 133998.
8 S.-Y. Ding, M. Dong, Y.-W. Wang, Y.-T. Chen, H.-Z. Wang, C.-Y. Su and W. Wang, *J. Am. Chem. Soc.*, 2016, **138**, 3031–3037.
9 S. Oh, J. Jeon, J. Jeong, J. Park, E.-T. Oh, H. J. Park and K.-H. Lee, *Anal. Chem.*, 2020, **92**, 4917–4925.
10 Q. Zhang, H. Ding, X. Xu, G. Liu and S. Pu, *Inorg. Chem. Commun.*, 2022, **139**, 109352.
11 C. Zhang, S. Nie, C. Liu, Y. Zhang and J. Guo, *J. Fluoresc.*, 2025, **35**, 2875–2884.
12 K. Prabakaran, H. Oh, R. Manivannan, S. Hyeong Park and Y.-A. Son, *Spectrochim. Acta, Part A*, 2022, **279**, 121437.
13 Y. Jiao, L. Zhou, H. He, J. Yin and C. Duan, *Talanta*, 2017, **162**, 403–407.
14 J. M. V. Ngororabanga, Z. R. Tshentu and N. Mama, *J. Fluoresc.*, 2020, **30**, 985–997.
15 A. Battison, S. Schoeman and N. Mama, *J. Fluoresc.*, 2023, **33**, 267–285.
16 Y. Ding, Y. Pan and Y. Han, *Ind. Eng. Chem. Res.*, 2019, **58**, 7786–7793.
17 N. K. Hien, M. V. Bay, N. C. Bao, Q. V. Vo, N. D. Cuong, T. V. Thien, N. T. A. Nhung, D. U. Van, P. C. Nam and D. T. Quang, *ACS Omega*, 2020, **5**, 21241–21249.
18 L. Wang, Y. Ma and W. Lin, *J. Hazard. Mater.*, 2024, **461**, 132604.
19 C.-Y. Li, F. Xu, Y.-F. Li, K. Zhou and Y. Zhou, *Anal. Chim. Acta*, 2012, **717**, 122–126.
20 A. I. Said, D. Staneva, S. Angelova and I. Grabchev, *Sensors*, 2023, **23**(1), 399–415.
21 M. Vedamalai and S.-P. Wu, *Org. Biomol. Chem.*, 2012, **10**, 5410–5416.
22 S. Routray, S. Acharya, L. Nayak, S. Pattnaik and R. Satapathy, *RSC Adv.*, 2025, **15**, 9910–9951.
23 P. Kaur and K. Singh, *J. Mater. Chem. C*, 2019, **7**, 11361–11405.

24 A. Maity, A. Sil, S. Nad and S. K. Patra, *Sens. Actuators, B*, 2018, **255**, 299–308.
25 L. Wang, G. Fang and D. Cao, *Sens. Actuators, B*, 2015, **207**, 849–857.
26 S. Khan, M. Muhammad, J. S. Algethami, H. M. Al-Saidi, A. Almahri and A. A. Hassanian, *J. Fluoresc.*, 2022, **32**, 1889–1898.
27 M. Hosseini, Z. Vaezi, M. R. Ganjali, F. Faridbod, S. D. Abkenar, K. Alizadeh and M. Salavati-Niasari, *Spectrochim. Acta, Part A*, 2010, **75**, 978–982.
28 D. Udhayakumari and V. Inbaraj, *J. Fluoresc.*, 2020, **30**, 1203–1223.
29 P. Mohanty, P. P. Dash, S. Mishra, R. Bhaskaran and B. R. Jali, *J. Fluoresc.*, 2025, **35**, 3181–3194.
30 F. U. Rahman, M. Bibi, E. Khan, A. B. Shah, M. Muhammad, M. N. Tahir, A. Shahzad, F. Ullah, M. Zahoor, S. Alamery and G. E.-S. Batiha, *Molecules*, 2021, **26**(15), 4506–4521.
31 M. Ghanei-Motlagh, M. Fayazi and M. A. Taher, *Sens. Actuators, B*, 2014, **199**, 133–141.
32 E. M. Bakir, A. R. Sayed and H. M. A. El-Lateef, *J. Photochem. Photobiol., A*, 2022, **422**, 113569.
33 T. Rasheed, M. Bilal, F. Nabeel, H. M. N. Iqbal, C. Li and Y. Zhou, *Sci. Total Environ.*, 2018, **615**, 476–485.
34 Y. Shen, X. Zhang, Y. Zhang, H. Li and Y. Chen, *Sens. Actuators, B*, 2018, **258**, 544–549.
35 G. He, Y. Zhao, C. He, Y. Liu and C. Duan, *Inorg. Chem.*, 2008, **47**, 5169–5176.
36 A. V. Raveendran, P. A. Sankeerthana, A. Jayaraj and P. Chinna Ayya Swamy, *Results Chem.*, 2022, **4**, 100297.
37 I. Esnal, G. Duran-Sampedro, A. R. Agarrabeitia, J. Bañuelos, I. García-Moreno, M. A. Macías, E. Peña-Cabrera, I. López-Arbeloa, S. de la Moya and M. J. Ortiz, *Phys. Chem. Chem. Phys.*, 2015, **17**, 8239–8247.
38 J. Sokołowska, W. Czajkowski and R. Podsiadły, *Dyes Pigm.*, 2001, **49**, 187–191.
39 F. Cicekbilek, B. Yilmaz, M. Bayrakci and O. Gezici, *J. Fluoresc.*, 2019, **29**, 1349–1358.
40 Y. Lv, D. Gao, Z. Di, M. Liu, H. Liu, M. Liu, Y. Yu and D. Song, *J. Hazard. Mater.*, 2025, **495**, 138928.
41 O. Sunnapu, N. G. Kotla, B. Maddiboyina, S. Singaravadivel and G. Sivaraman, *RSC Adv.*, 2016, **6**, 656–660.
42 R. V. Rathod, S. Bera, P. Maity and D. Mondal, *ACS Omega*, 2020, **5**, 4982–4990.
43 J. B. Chae, D. Yun, H. Lee, H. Lee, K.-T. Kim and C. Kim, *ACS Omega*, 2019, **4**, 12537–12543.
44 S. Liu, X. Zhang, C. Yan, P. Zhou, L. Zhang, Q. Li, R. Zhang, L. Chen and L. Zhang, *J. Hazard. Mater.*, 2022, **424**, 127701.
45 S. O. Fakayode, C. Lisse, W. Medawala, P. N. Brady, D. K. Bwambok, D. Anum, T. Alonge, M. E. Taylor, G. A. Baker, T. F. Mehari, J. D. Rodriguez, B. Elzey, N. Siraj, S. Macchi, T. Le, M. Forson, M. Bashiru, V. E. Fernand Narcisse and C. Grant, *Appl. Spectrosc. Rev.*, 2024, **59**, 1–89.
46 G. Sathiyan, G. Venkatesan, S. K. Ramasamy, J. Lee and S. Barathi, *J. Environ. Chem. Eng.*, 2024, **12**, 112804.
47 A. Chakraborty and N. Das, *Eur. J. Inorg. Chem.*, 2025, e202400717.
48 S. Chakraborty, S. Goswami, C. K. Quah and B. Pakhira, *R. Soc. Open Sci.*, 2018, **5**, 180149.
49 L. Wu, A. C. Sedgwick, X. Sun, S. D. Bull, X.-P. He and T. D. James, *Acc. Chem. Res.*, 2019, **52**, 2582–2597.
50 A. Habibalahi, M. D. Moghari, J. M. Campbell, A. G. Anwer, S. B. Mahbub, M. Gosnell, S. Saad, C. Pollock and E. M. Goldys, *Redox Biol.*, 2020, **34**, 101561.
51 N. Ercal, H. Gurer-Orhan and N. Aykin-Burns, *Curr. Top. Med. Chem.*, 2001, **1**, 529–539.
52 F. Wang, B. Zeng, Z. Sun and C. Zhu, *Arch. Environ. Contam. Toxicol.*, 2009, **56**, 723–731.
53 J. Xiao, S. Guo, D. Wang and Q. An, *Chem. – Eur. J.*, 2024, **30**, e202304337.
54 A. Ruggi, F. W. B. van Leeuwen and A. H. Velders, *Coord. Chem. Rev.*, 2011, **255**, 2542–2554.
55 S. Fooladi, M. H. Nematollahi and S. Iravani, *Environ. Res.*, 2023, **231**, 116287.
56 Z. Zhou, J. Song, L. Nie and X. Chen, *Chem. Soc. Rev.*, 2016, **45**, 6597–6626.
57 J.-T. Hou, K.-K. Yu, K. Sunwoo, W. Y. Kim, S. Koo, J. Wang, W. X. Ren, S. Wang, X.-Q. Yu and J. S. Kim, *Chem*, 2020, **6**, 832–866.
58 D. Pelinescu, M. Anastasescu, V. Bratan, V.-A. Maraloiu, C. Negrila, D. Mitrea, J. Calderon-Moreno, S. Preda, I. C. Gîfu, A. Stan, R. Ionescu, I. Stoica, C. Anastasescu, M. Zaharescu and I. Balint, *Gels*, 2023, **9**(8), 650–671.
59 I. Albesa, M. C. Becerra, P. C. Battán and P. L. Páez, *Biochem. Biophys. Res. Commun.*, 2004, **317**, 605–609.
60 M. A. Quinteros, V. Cano Aristizábal, P. R. Dalmasso, M. G. Paraje and P. L. Páez, *Toxicol. In Vitro*, 2016, **36**, 216–223.
61 E. Antina, N. Bumagina, Y. Marfin, G. Guseva, L. Nikitina, D. Sbytov and F. Telegin, *Molecules*, 2022, **27**(4), 1396–1454.
62 N. Tsolekile, S. Nelana and O. S. Oluwafemi, *Molecules*, 2019, **24**(14), 2669–2683.
63 F. Schmitt, P. Govindaswamy, G. Süss-Fink, W. H. Ang, P. J. Dyson, L. Juillerat-Jeanneret and B. Therrien, *J. Med. Chem.*, 2008, **51**, 1811–1816.
64 K. Lin, Z.-Z. Zhao, H.-B. Bo, X.-J. Hao and J.-Q. Wang, *Front. Pharmacol.*, 2018, **9**, 1323.
65 S. Zeng, X. Liu, Y. S. Kafuti, H. Kim, J. Wang, X. Peng, H. Li and J. Yoon, *Chem. Soc. Rev.*, 2023, **52**, 5607–5651.
66 M. Delwar Hossain, R. K. Pandey, U. Rana and M. Higuchi, *J. Mater. Chem. C*, 2015, **3**, 12186–12191.
67 M. Sasmal, R. Bhowmick, A. S. Musha Islam, S. Bhuiya, S. Das and M. Ali, *ACS Omega*, 2018, **3**, 6293–6304.
68 A. M. Brouwer, *Pure Appl. Chem.*, 2011, **83**(12), 2213–2228.
69 M. Singh, S. Senthilkumar, S. Rajput and S. Neogi, *Inorg. Chem.*, 2020, **59**, 3012–3025.
70 P. Samanta, A. V. Desai, S. Sharma, P. Chandra and S. K. Ghosh, *Inorg. Chem.*, 2018, **57**, 2360–2364.
71 S. Sasan, T. Chopra, A. Gupta, D. Tsering, K. K. Kapoor and R. Parkesh, *ACS Omega*, 2022, **7**, 11114–11125.
72 K. Aich, S. Goswami, S. Das and C. D. Mukhopadhyay, *RSC Adv.*, 2015, **5**, 31189–31194.
73 G. Routholla, S. Pulya, T. Patel, S. Abdul Amin, N. Adhikari, S. Biswas, T. Jha and B. Ghosh, *Bioorg. Chem.*, 2021, **114**, 105050.
74 G. Routholla, S. Pulya, T. Patel, N. Adhikari, S. Abdul Amin, M. Paul, S. Bhagavatula, S. Biswas, T. Jha and B. Ghosh, *Bioorg. Chem.*, 2021, **117**, 105446.

75 S. Pulya, A. Himaja, M. Paul, N. Adhikari, S. Banerjee, G. Routholla, S. Biswas, T. Jha and B. Ghosh, *J. Med. Chem.*, 2023, **66**, 12033–12058.

76 S. Pulya, T. Patel, M. Paul, N. Adhikari, S. Banerjee, G. Routholla, S. Biswas, T. Jha and B. Ghosh, *Eur. J. Med. Chem.*, 2022, **238**, 114470.

77 S. K. Baidya, T. Patel, A. Himaja, S. Banerjee, S. Das, B. Ghosh, T. Jha and N. Adhikari, *Drug Dev. Res.*, 2024, **85**, e22255.

78 A. Maji, A. Himaja, S. Nikhitha, S. Rana, A. Paul, A. Samanta, U. Shee, C. Mukhopadhyay, B. Ghosh and T. K. Maity, *RSC Med. Chem.*, 2024, **15**, 3057–3069.

79 A. Chakraborty, V. K. Rajana, C. Saritha, A. Srivastava, D. Mandal and N. Das, *J. Hazard. Mater.*, 2024, **470**, 134207.

80 A. Chakraborty, C. Jaiswal, A. Hassan, S. Kumar, K. Singh, B. B. Mandal and N. Das, *Appl. Organomet. Chem.*, 2022, **36**(7), e6711.

81 A. Chakraborty, K. Singh, P. Vaswani, A. Gangrade, D. Bhatia and N. Das, *Appl. Organomet. Chem.*, 2023, **37**(8), e7172.

82 S. K. Baidya, T. Patel, A. Himaja, S. Banerjee, S. Das, B. Ghosh, T. Jha and N. Adhikari, *J. Mol. Struct.*, 2025, **1328**, 141278.

83 A. Chakraborty, S. Pandey, R. K. Pandey, K. Singh, S. Kumar, S. Kumar, T. R. Rao and N. Das, *Appl. Organomet. Chem.*, 2023, **37**(1), e6917.

84 J. S. Renny, L. L. Tomasevich, E. H. Tallmadge and D. B. Collum, *Angew. Chem., Int. Ed.*, 2013, **52**, 11998–12013.

85 Y. Liu, P. Zhou, Y. Wu, X. Su, H. Liu, G. Zhu and Q. Zhou, *Sci. Total Environ.*, 2022, **827**, 154357.

86 M. Ozdemir, *Sens. Actuators, B*, 2017, **249**, 217–228.

87 A. Chakraborty, S. Bhar, B. Kumar, A. Chandra and N. Das, *Appl. Organomet. Chem.*, 2025, **39**(12), e70430.